

Probing atomic ordering and multiple twinning in metal nanocrystals through their vibrations

H. Portales^{*†}, N. Goubet^{*†}, L. Saviot[‡], S. Adichtchev[§], D. B. Murray[¶], A. Mermet[§], E. Duval[§], and M.-P. Pileni^{*†||}

^{*}Université Pierre et Marie Curie Paris 6, and [†]Centre National de la Recherche Scientifique, Unité Mixte de Recherche 7070, LM2N, 4 Place Jussieu, F-75005 Paris, France; [‡]Institut Carnot de Bourgogne, Unité Mixte de Recherche 5209, Centre National de la Recherche Scientifique, Université de Bourgogne, 9 Avenue A. Savary, BP 47870, F-21078 Dijon Cedex, France; [§]Laboratoire de Physico-Chimie des Matériaux Luminescents, Université Lyon 1, Unité Mixte de Recherche 5620, Centre National de la Recherche Scientifique, Bât. A. Kastler, 10 Rue Ampère, F-69622 Villeurbanne, France; and [¶]Mathematics, Statistics, and Physics Unit, University of British Columbia Okanagan, 3333 University Way, Kelowna, BC, Canada V1V 1V7

Edited by Louis E. Brus, Columbia University, New York, NY, and approved August 6, 2008 (received for review April 17, 2008)

Control of nanocrystal (NC) crystallinity currently raises great interest because of its potential benefits in both physics modeling and technological applications. Advances in methods for synthesizing perfect single-crystalline NCs are recent, so that the effect of crystallinity on NC properties has received only limited study and still needs to be properly investigated. Here, we report that crystallinity of gold NCs dramatically modifies their vibrations. Using low-frequency Raman scattering, we clearly demonstrate that single-domain NCs vibrate differently than their multiply twinned counterparts, through the splitting of the quadrupolar vibrations, which is only observed for the former. Using the resonant ultrasound approach, we calculate the vibrational frequencies of a gold sphere and show that elastic anisotropy induces a lift of degeneracy of the quadrupolar mode in good agreement with our experimental measurements. These findings open up challenging perspectives on using Raman spectroscopy to characterize nanocrystallinity.

crystallinity | elastic anisotropy | quadrupolar mode | Raman spectroscopy

Crystallinity was recently shown to have an effect on the reactivity, the electron-phonon interaction, and the mechanical properties of silver nanocrystals (NCs), in this way demonstrating perfect nanocrystallinity to be a relevant issue in tailoring NCs' properties (1). From a theoretical point of view, atomistic simulations have pointed out some specific effects of morphology on phonons in nanoscopic metal grains (2), showing that realistic nanograin models display complex vibrational properties. As a counterpart to the simulations, very few experimental investigations have been reported that attempt to demonstrate such a dependence of vibrational properties on the degree of crystallinity of metal NCs (1, 3). This is partially due to the difficulty in tailoring the crystallinity of NCs, as mentioned above, but also to the technical limitation in detecting and identifying the related experimental features. The present article reports that vibrational properties of noble-metal NCs dramatically depend on their nanocrystallinity and clearly demonstrates the relevance of elastic anisotropy in small NCs. These findings make it possible to use vibrational spectroscopy as an alternative or complementary nondestructive tool to the electron microscopy techniques for characterizing nanocrystallinity and also provide interesting insights for understanding, at the nanoscale, how vibrations are affected by the presence of twinning planar defects in metal NCs.

Results and Discussion

In this work, we use a one-step one-phase synthetic route (4) to produce colloidal solutions containing gold NCs. Several samples are synthesized by depositing the NCs on a substrate of highly oriented pyrolytic graphite (HOPG). These samples mainly contain single-domain gold NCs with a size distribution slightly varying from one sample to the other. In these samples, NCs tend to spontaneously self-organize because of their very narrow size distribution [see [supporting information \(SI\) Fig.](#)

[S1](#)]. Samples made with gold NCs having mean diameters (and polydispersity) of 5.3 nm (6%), 5.1 nm (6%), and 4.3 nm (7%) will be indicated in the following as *Au(5.3)*, *Au(5.1)* and *Au(4.3)*, respectively. The mean diameter D_{TEM} and the polydispersity are deduced for each sample from a fit of the corresponding histogram by using a Gaussian profile. The values of D_{TEM} are reported in Table 1. Fig. 1 shows the high-resolution transmission electron microscopy (HRTEM) image of gold NCs used to produce sample *Au(5.3)*. From this image, it is obvious that most gold NCs are single domain, as, for example, the crystal "1," whose power spectrum (*Inset 1* of Fig. 1) indicates an orientation along the [110] direction (5). In parallel, only a few of the NCs appear with internal defects such as crystal "2." The arrangement of the spots in the corresponding power spectrum (*Inset 2* of Fig. 1) indicates this NC to be formed by several domains. NCs for which no atomic planes are distinguished in the HRTEM image, such as crystal "3," are potentially single domain. In such a case, the apparent absence of any lattice fringe is due only to misorientation. As a consequence, no spot is observed on the power spectrum (*Inset 3* of Fig. 1). This result is confirmed from a large population of gold NCs through the quantification of their domain size by performing x-ray diffraction measurements and then by analyzing the XRD diffractograms (see [SI Text](#) and [Fig. S2](#)). The diameters deduced by this technique for samples *Au(5.3)* and *Au(4.3)* are found to be 5.2 nm and 4.1 nm, respectively, which is in good agreement with those estimated from TEM analysis and well confirms that gold NCs are single domain.

Fig. 2*a* shows the low-frequency Stokes/anti-Stokes Raman spectrum of sample *Au(5.1)*. This spectrum exhibits a very unusual profile with two sharp bands of comparable intensities showing up at 156 and 229 GHz. The higher-frequency band appears to be asymmetric and broader than the former. For convenience, these two bands will be indicated in the following as "B1" and "B2," respectively. The observation of such a double band is surprising because it is in contrast with results commonly obtained by low-frequency Raman scattering (LFRS) from self-organized metal NCs, where only one single band related to the quadrupolar vibrational mode of the NCs is observed (6). As a comparison, Fig. 2*b* shows a typical LFRS spectrum of gold NCs. This last spectrum was measured from sample *Au(5.8)* in which both single- and polycrystalline gold NCs coexist but with a much higher amount of the latter ones and a quite large

Author contributions: H.P., L.S., D.B.M., A.M., E.D., and M.-P.P. designed research; H.P., N.G., L.S., and S.A. performed research; H.P., N.G., L.S., A.M., and E.D. analyzed data; and H.P., N.G., and D.B.M. wrote the paper.

The authors declare no conflict of interest.

This article is a PNAS Direct Submission.

||To whom correspondence should be addressed. E-mail: pileni@sri.jussieu.fr.

This article contains supporting information online at www.pnas.org/cgi/content/full/0803748105/DCSupplemental.

© 2008 by The National Academy of Sciences of the USA

Table 1. Comparison of the vibrational frequencies of gold nanocrystals experimentally measured by LFRS with those calculated by using the RUS approach for the fivefold quadrupolar mode of a directionally averaged isotropic gold sphere and for the twofold E_g and threefold T_{2g} degenerate modes of an elastically anisotropic gold sphere

Sample	D_{TEM} , nm	Isotropic		Anisotropic		Experiment frequency, GHz
		Mode	Frequency, GHz (degeneracy)	Mode	Frequency, GHz (degeneracy)	
<i>Au(5.3)</i>	5.3	$l=2, n=0$	$197 (\times 5)$	E_g	$139 (\times 2)$	140
				T_{2g}	$225 (\times 3)$	211
<i>Au(5.1)</i>	5.1	$l=2, n=0$	$206 (\times 5)$	E_g	$146 (\times 2)$	156
				T_{2g}	$235 (\times 3)$	229
<i>Au(4.3)</i>	4.3	$l=2, n=0$	$243 (\times 5)$	E_g	$172 (\times 2)$	168
				T_{2g}	$277 (\times 3)$	253

polydispersity of $\approx 13\%$ (see Fig. S1). In the spectrum of sample *Au(5.1)*, we also observe other much less intense peaks at 353, 424, and 590 GHz (marked with asterisks in Fig. 2a) whose origin is attributed to scattering from air (rotations of O₂ and N₂ molecules).

A pertinent pathway to go further consists, therefore, in studying the Raman scattering by gold NCs of different sizes. This procedure aims to reveal some dependence of the measured LFRS signal on the NC size, as is usually observed in Raman scattering by the vibrations of NCs (7, 8). The Stokes/anti-Stokes low-frequency Raman spectra of all samples are shown in Fig. 2c. As is apparent from this figure, both the B1 and B2 bands shift toward higher frequencies for decreasing NC size, from *Au*(5.3) to *Au*(4.3). These frequencies vary as the inverse of the NC diameter. This follows from comparing the ratio of the NC diameters in the two samples with those of the frequencies measured at the band maximum. Such a size dependence of the frequencies measured at the maximum of both B1 and B2 bands make it then possible to accurately assign these two bands to LFRS by the vibrations of gold NCs.

To avoid any ambiguous identification of the vibrational modes revealed in the LFRS spectra of single-domain gold NCs, we have to consider all of the mechanisms that could potentially explain the origin of the double band. From the well established dependence of Raman scattering on either size or shape of metal NCs (7–9), a bimodal size distribution or a shape anisotropy of the NCs are both expected to result in the observation of a

double band in the LFRS spectrum. However, because on one hand, all gold NC size distributions clearly exhibit a single Gaussian profile (see Fig. S1), and, on the other hand, because HRTEM images reveal the shape of most NCs to be quasispherical (Fig. 1), neither bimodality of the NC size distribution nor the NC shape anisotropy can be invoked to explain the double band. Besides, such a double band has been observed from both disordered and well organized assemblies of gold NCs without any noticeable difference in the position and width of the Raman bands, thereby ruling out any possible effect of vibrational coherence as those being theoretically predicted (10) and already observed (11) in cubic face-centered supracrystals of silver NCs. A further possibility has still to be invoked to explain the double band through the potential effect of an interaction between the particles and the substrate. Orrit and coworkers (12) have already shown this effect to permit the detection of the (non-spherically symmetric) $l = 2$ quadrupolar mode of gold particles in their single-particle transient absorption measurements (normally only isotropic modes are observed in transient absorption experiments on metal nanoparticles). Nevertheless, if this effect was significant, then it should also be observed for the polycrystalline NCs. Thus, we rule out such a phenomenon to be the cause of the double band. At this point, the crystallinity of the gold NCs appears likely to be at the origin of the double band in the LFRS spectra. The theoretical arguments and computational calculations of vibrational frequencies of gold spheres that follow strongly support the argument in favor of this assumption.

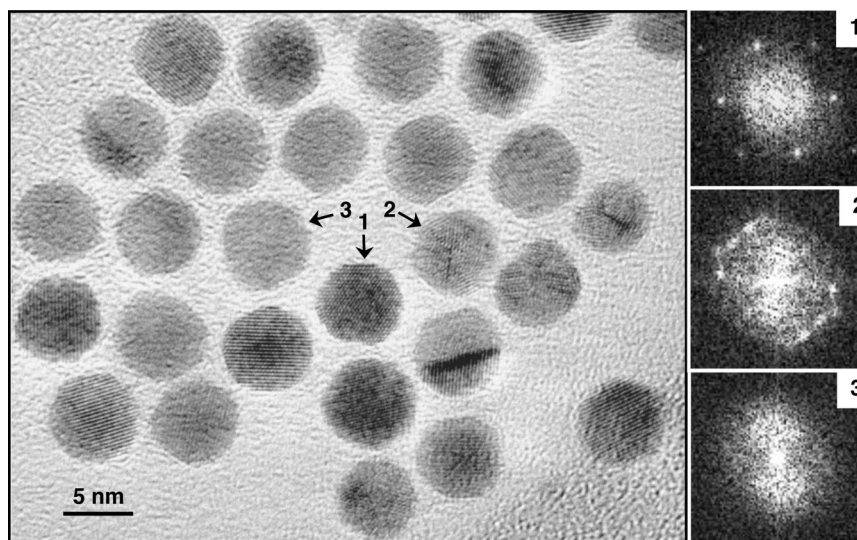


Fig. 1. HRTEM image and power spectra of gold NCs from sample Au(5.3). On the right side are shown the power spectra of the gold NCs indicated by marks 1–3 on the HRTEM image.

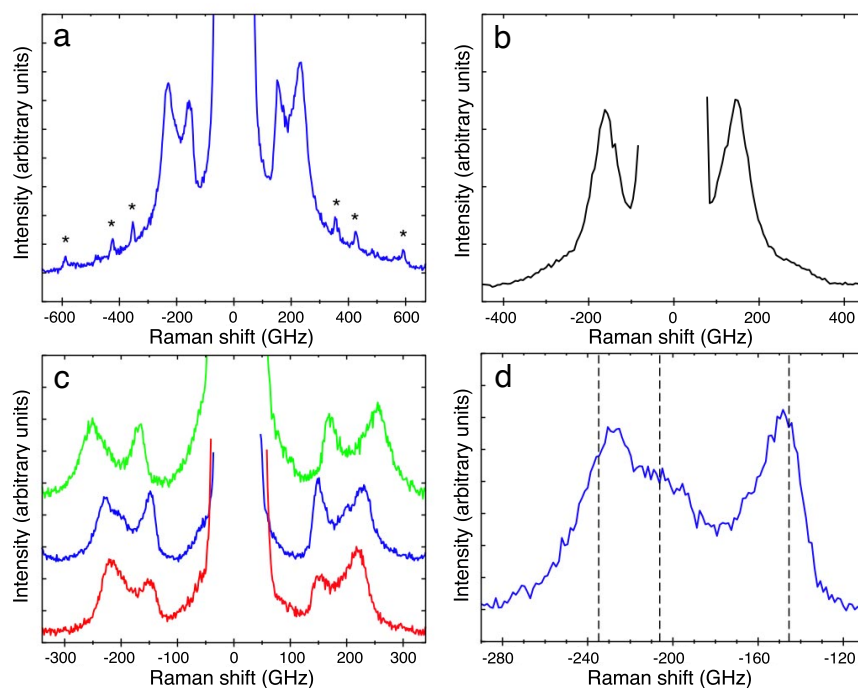


Fig. 2. Stokes/anti-Stokes LFRS spectra of gold NCs. (a) LFRS of sample Au(5.1) where features indicated by asterisks are likely to be due to light scattering by molecules from air that are adsorbed on the sample. (b) LFRS spectrum of multiply twinned gold NCs from sample Au(5.8). (c) Comparison of Stokes/anti-Stokes LFRS spectra of samples Au(5.3) (red curve), Au(5.1) (blue curve), and Au(4.3) (green curve), illustrating the dependence of the LFRS signal on the size of the NCs. (d) Anti-Stokes LFRS spectrum of sample Au(5.1) clearly showing the structured profile of the double band. Dashed lines are vertically plotted to indicate the vibrational frequencies of gold NCs of 5.1 nm in diameter, as calculated for the T_{2g} , the $l = 2$ quadrupolar, and the E_g modes (in decreasing order of Raman shifts). Spectra in C have been vertically shifted and amplitudes independently scaled for clarity.

The standard theory used to predict the frequencies of the vibration of nanoparticles was introduced by Lamb (13) more than a century ago. This approach is based on the continuum approximation and assumes that the nanoparticles have a spherical shape and also that their elasticity is isotropic. To go beyond this last limitation, it is necessary to use a numerical approach. In this work, we used the resonant ultrasound (RUS) approach (14). The results were double checked both with the Lamb's model for isotropic system and with a finite element mesh sequence (FEMS) approach (15). Double checking with this last method is a very important step because it is easy to design systems for which the convergence of the RUS algorithm is very slow. It was thus essential to check that the high anisotropy of gold (Zener factor: 2.92) does not trigger this behavior.

The elastic tensor for gold used here is defined by $C_{11} = 191$ GPa, $C_{12} = 162$ GPa, $C_{44} = 42.4$ GPa. The mass density (16) is 19.283 g/cm³. To account for the twinning of the NCs, we used an isotropic approximation of gold with three-dimensional averaged sound velocities, i.e.: $\langle v_L \rangle = 3,330$ m/s and $\langle v_T \rangle = 1,250$ m/s. We do not expect individual NCs in our samples to oscillate as isotropic spheres. However, the twinned NCs are all different because they do not have the same number or location of twins. Therefore, we consider that the isotropic approximation provides a good description of this ensemble. The same approximation has been used successfully up to now to model the Raman measurements on NCs with uncontrolled crystallinity. To emphasize this point in the following, we will refer to the twinned NCs as fictive isotropic spheres.

It is expected, on the basis of group theoretical considerations (17) and confirmed by RUS calculations, that the fivefold degenerate spheroidal $l = 2$ mode of an elastically isotropic sphere is broken into two different levels by lowering the elastic symmetry to that of a cubic crystal. The corresponding representations are E_g (degeneracy two) and T_{2g} (degeneracy three).

Interestingly, by using RUS, this lifting of degeneracy can be progressively followed by varying the elastic tensor C_{ij} of gold spheres expressed here as a linear combination of the elastic tensors of a “fictive” fully isotropic gold sphere, $C_{ij}^{[I]}$, and a perfectly anisotropic one, $C_{ij}^{[A]}$:

$$C_{ij} = (1 - x)C_{ij}^{[I]} + xC_{ij}^{[A]} \quad [1]$$

where x is real, ranging between 0 and 1. The splitting of the quadrupolar mode is illustrated in Fig. 3, which shows the

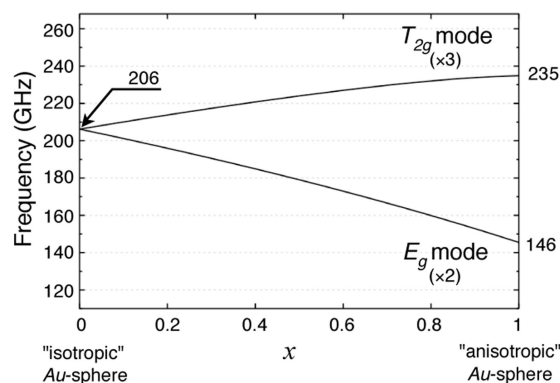


Fig. 3. Splitting of the quadrupolar vibrational mode due to elastic anisotropy in a gold sphere of 5.1 nm in diameter. The plotted curves show the dependence of the $l = 2$ quadrupolar mode on the gold elastic anisotropy when the elastic tensor of gold is linearly varied according to Eq. 1: From the case of a directionally averaged “isotropic” metal ($x = 0$) to the one of a truly “anisotropic” medium ($x = 1$), the fivefold degenerate $l = 2$ mode of the gold sphere splits into two different levels corresponding to the twofold E_g and threefold T_{2g} degenerate modes.

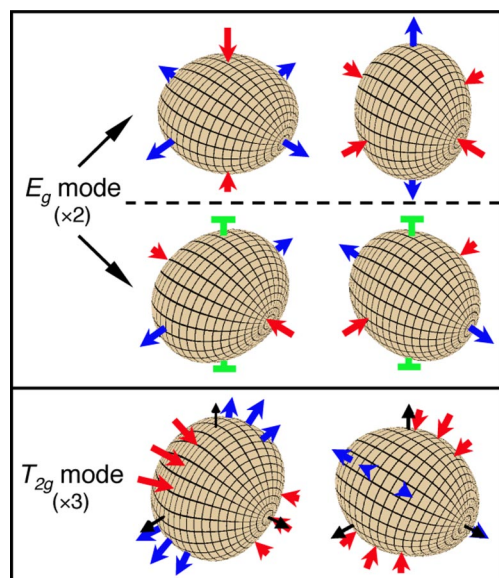


Fig. 4. Schematic representation of the motions of a gold sphere for different vibrational modes. From top to bottom, the two E_g modes and one of the three T_{2g} modes are shown. Other T_{2g} modes are obtained by cyclic permutations of the three axes. In these pictures, arrows of different colors are used to represent either compression (red arrows) or expansion (blue arrows) motions of the sphere. Green symbols designate quasifixed points on the surface of the sphere, i.e., places where displacements are very limited in amplitude.

dependence of the vibrational frequencies of a gold sphere versus the variation of the gold elastic anisotropy.

It is worth noting that, even if the HRTEM images clearly reveal that most gold NCs are faceted, the same splitting was calculated (with deviations of the ratio of the T_{2g} and E_g frequencies $<4\%$) for NCs having spherical or polyhedral shape (cuboctahedra and truncated cuboctahedra), at variance with a previous report (17). A schematic representation of the motions of a vibrating sphere involved in few selected modes is given in

Fig. 4 (see also dynamical representations in [Movie S1](#), [Movie S2](#), [Movie S3](#), [Movie S4](#), and [Movie S5](#)). Note that for these modes, the displacements are almost identical for isotropic and anisotropic gold spheres, yet the frequencies are significantly different (Fig. 3).

The vibrational frequencies of gold NCs measured by LFRS from three different samples are listed in Table 1 and compared with those calculated by using RUS for both isotropic and anisotropic gold spheres with a size corresponding for each sample to the mean diameter D_{TEM} . From this comparison, the frequencies measured at the maximum of the two bands are in reasonable agreement with those calculated for the E_g and T_{2g} modes of a gold anisotropic sphere. A close inspection of the LFRS spectrum of sample *Au(5.1)* plotted in Fig. 2d not only well illustrates this result but also reveals the profile of the double band to be structured, with a shoulder at ≈ 200 GHz making the band B2 to appear asymmetric. This last frequency well matches that of the fivefold degenerate quadrupolar mode from a fictive isotropic gold sphere. Therefore, the several components of the LFRS (Fig. 2d) from the NC assemblies displayed in Fig. 1 can be interpreted through the following assignments: The band B1 corresponds to the scattering by the E_g mode of single-domain gold NCs. The band B2 and its shoulder on the low-frequency side are ascribed to the respective contributions of single- and polycrystalline NCs to the LFRS signal. This assumption makes sense because, even if gold NCs are mainly single domain in the samples from which the double band is observed, some other polycrystalline NCs also coexist in these samples, as clearly seen in Fig. 1 for the case of sample *Au(5.1)*, and obviously contribute to the detected LFRS signal.

Finally, to confirm the crucial role of the NC crystallinity, and equivalently, of the elastic anisotropy, on our ability to observe the splitting of the quadrupolar mode, we present some results obtained from NCs with many more internal twinning defects as compared with the single-domain gold NCs. These NCs are made of silver, which should compare well with gold in terms of elastic anisotropy. The silver NCs under consideration here were produced by using a ripening route (see *Methods*). The corresponding sample *Ag(5.1)* was synthesized with silver NCs having a mean diameter of 5.1 nm and a size distribution (Fig. 5*b*) as narrow as that obtained in the samples of single-domain gold NCs. Unlike the aforementioned gold NCs, the HRTEM image

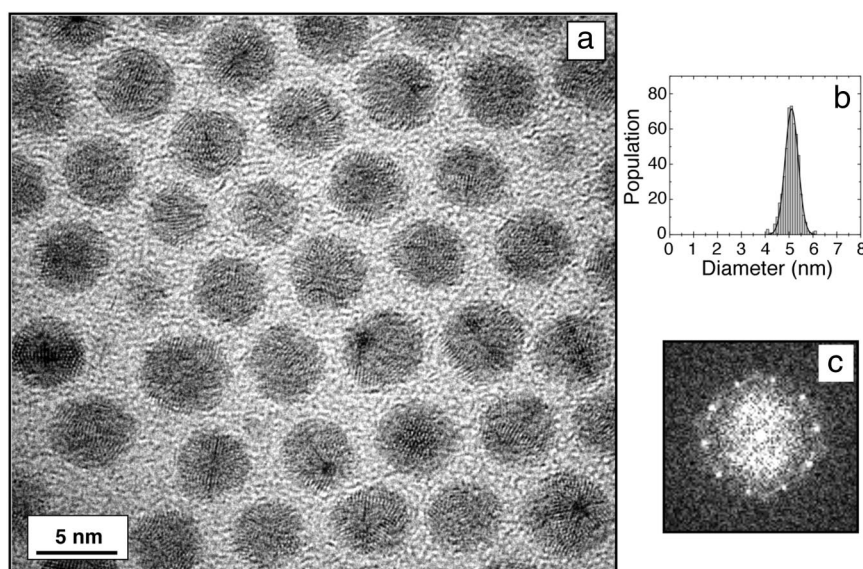


Fig. 5. HRTEM characterization of silver MTPs. (a and b) HRTEM image (a) and size distribution (b) histogram of multiply twinned silver NCs from sample AG(5.1). The size distribution histogram is determined from >500 silver NCs from the colloidal solution used to produce sample AG(5.1). (c) Power spectrum as typically obtained from a silver icosahedron oriented along the fivefold axis.

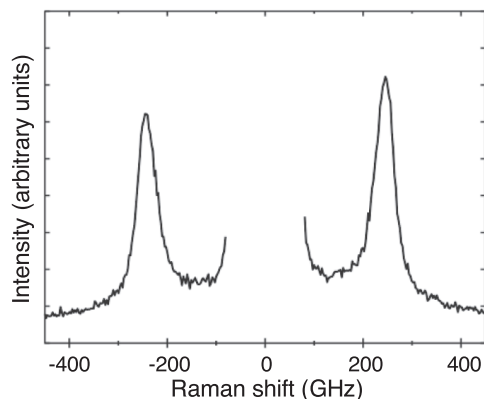


Fig. 6. Stokes/anti-Stokes LFRS spectrum of multiply twinned silver NCs measured from sample AG(5.1).

reveals that the silver NCs bear many defects, like twins (Fig. 5a). In most cases, these silver NCs are made with several domains, which have joined themselves according to different symmetrical arrangements, forming multiply twinned particles (MTPs) (18), such as decahedra or icosahedra (Fig. 5c). In contrast with the results obtained from single-domain gold NCs, the Raman spectrum of sample Ag(5.1) exhibits, at very low Raman shift (<500 GHz), only one high-intensity band (Fig. 6), centered at 244 GHz. This unique band corresponds to the global contribution of MTPs to the Raman spectrum, similar to what is observed from sample Au(5.8) (Fig. 2b). In both cases, only one band is observed because of the inhomogeneous broadening that is inherent to the large variety of nanocrystalline structures in the population of the multiply twinned NCs. This clearly confirms that no splitting of the quadrupolar mode is observable when mainly MTPs are involved in the light-scattering mechanism. Moreover, when such a splitting is observed, it acts as a reliable indicator of the good nanocrystallinity of the NCs from which the LFRS is coming, most of them being, therefore, single-domain NCs.

As shown in this article, the low-frequency vibrational modes of metal NCs exhibit a strong dependence on their nanocrystallinity. The quality of the atomic ordering, through its associated elastic properties, sensitively affects the vibrations of metal NCs, enabling the clear observation by Raman scattering of a splitting of the intense quadrupolar mode when NCs are mainly single domain, whereas no splitting is observed for their multiply twinned counterparts. In the recent past, some of us have observed coherence effects on Raman scattering (10, 11) from NCs self-organized in face centered cubic supracrystals. Properly controlling the supracrystallinity in such three-dimensional assemblies of NCs could open up challenging perspectives in exploiting the potential effect of elastic anisotropy on collective vibrational properties.

Methods

Syntheses of Single-Domain Gold NCs and Silver MTPs. Single-domain gold NCs are synthesized by using a modified Stucky's protocol (4). Briefly, we first dissolve 0.25 mM AuPPH₃Cl in 25 ml of toluene for both samples Au(5.3) and

Au(5.1) and 22 ml for sample Au(4.3), and then, dodecanethiol (2 mM) is added to the solution. The metal precursor is reduced by using two different solutions of tert-butylamine borane complex in toluene: 5 ml at 1.0 mol/liter for both Au(5.3) and Au(5.1) and 2 ml at 2.5 mol/liter for Au(4.3). During the synthesis, the temperature is fixed at 100°C.

Sample Au(5.8) is synthesized by using a modified Brust's protocol (19). Briefly, an aqueous solution (30 ml) containing 3 mM HAuCl₄·3H₂O is added to 80 ml of tetradecylammonium bromide (TDAB) in toluene at 50 mM. After 10 min of stirring, the organic phase turns to orange color, and the colorless aqueous phase is removed. Sodium borohydride aqueous solution (25 ml) at 0.4 M is added, and the biphasic system is stirred. After 3 h, the aqueous solution is removed as above, and 1-dodecanethiol (4.2 mM) is added to the organic phase. The solvent in the organic phase is fully evaporated in a rotary evaporator and the crude solid is dried under vacuum overnight. The solid is dissolved in 5 ml of toluene, and the concentrated solution is then annealed progressively with a heating rate of 10°C·min⁻¹. After a few minutes, the solution temperature reaches 160°C and is kept at such a temperature for 30 min. At the end of the thermal process, the product reaches room temperature and is then dissolved in toluene.

For the synthesis of silver MTPs, chlorotris(triphenylphosphine)silver is used as the metal precursor. A solution of this precursor at 0.01 M is mixed with 2 mM dodecanethiol. A solution of tert-butylamine borane complex at 0.17 M is then added for the reduction. After 3 h, some small particles (<2 nm) start to appear in the solution and progressively grow so that, 3 h later, the diameter of the larger NCs is ≈ 5 nm. After leaving the solution to stir overnight, NCs of ≈ 5 nm in diameter with very narrow size distribution are obtained and then used to synthesize sample Ag(5.1).

For both the syntheses of gold and silver NCs, we take care to wash the NCs with ethanol at the end of reduction to eliminate by-products, and we finally disperse them in neat toluene.

Transmission Electron Microscopy Analyses. Conventional transmission electron microscopy is performed by operating a JEOL 1011 (100 kV) microscope, and HRTEM images are taken from a JEOL 2010 (200 kV). For these TEM analyses, samples are prepared by dissolving the NCs in hexane or in toluene, and then the obtained NC solution is drop cast onto a carbon-coated copper grid (200-mesh).

Powder X-Ray Diffraction (XRD) Measurements. All XRD measurements are performed in transmittance mode by using a Siemens Kristalloflex diffractometer with a STOE goniometer (Co K α , $\lambda = 1.7902$ Å). The NCs are dropped on an x-ray transparent tape in concentrated solution. The data are collected within the 2θ -angle range of 35–110°. The scan data collection is carried out with a slow rate (60 s for each step of 0.1°) because of the weak intensity of the diffraction signal from the nanocrystallites.

Measurements of LFRS Spectra. All LFRS experiments are performed at room temperature on silver or gold NCs deposited on a highly oriented pyrolytic graphite substrate. For the excitation, monochromatic light at 532 nm is provided by a continuous yttrium aluminum garnet (YAG) laser. To prevent any damage to the sample that could arise from its long-duration laser irradiation, the incoming laser beam is focused on the surface of the sample at low optical intensity whose order of magnitude is limited to 10⁷ W/m². In most cases, LFRS spectra are recorded in a classical back-scattering geometry with a six-pass tandem Fabry-Pérot interferometer (20). Because of the low signal detected from our sample, a typical integration time of several hours was needed for each spectrum to get high signal-to-noise ratio. After such a long period under laser exposure, the irradiated sample was checked to be undamaged through the constant profile of the detected LFRS bands, attesting to the reproducibility of our results. The spectrum of sample Au(5.8) is obtained with a quintuple monochromator (Dilor Z40), at 90° from the incident light beam, and using the line at 647 nm of an Ar⁺ laser as the excitation source.

1. Tang Y, Ouyang M (2007) Tailoring properties and functionalities of metal nanoparticles through crystallinity engineering. *Nat Mater* 6:754–759.
2. Narvaez GA, Kim J, Wilkins JW (2005) Effects of morphology on phonons in nanoscopic silver grains. *Phys Rev B* 72:155411.
3. Duval E, et al. (2001) Spatial coherence effect on the low-frequency Raman scattering from metallic nanoclusters. *Phys Rev B* 63:075405.
4. Zheng N, Fan J, Stucky GD (2006) One-step one-phase synthesis of monodisperse noble-metallic nanoparticles and their colloidal crystals. *J Am Chem Soc* 128:6550–6551.
5. Urban J (1998) Crystallography of clusters. *Cryst Res Technol* 33:1009–1024.
6. Courty A, Lisiecki I, Pileni M-P (2002) Vibration of self-organized silver nanocrystals. *J Chem Phys* 116:8074–8078.

7. Palpant B, et al. (1999) Quadrupolar vibrational mode of silver clusters from plasmon-assisted Raman scattering. *Phys Rev B* 60:17107–17111.
8. Duval E, Boukenter A, Champagnon B (1986) Vibration eigenmodes and size of microcrystallites in glass: Observation by very-low-frequency Raman scattering. *Phys Rev Lett* 56:2052–2055.
9. Margueritat J, et al. (2006) Surface plasmons and vibrations of self-assembled silver nanocolumns. *Nano Lett* 6:2037–2042.
10. Duval E, Mermet A, Courty A, Albouy P-A, Pileni M-P (2005) Coherence effects on Raman scattering from self-organized Ag nanocrystals: Theory. *Phys Rev B* 72:085439.
11. Courty A, Mermet A, Albouy P-A, Duval E, Pileni M-P (2005) Vibrational coherence of self-organized silver nanocrystals in f.c.c. supra-crystals. *Nat Mater* 4:395–398.

12. Van Dijk MA, Lippitz M, Orrit M (2005) Detection of acoustic oscillations of single gold nanospheres by time-resolved interferometry. *Phys Rev Lett* 95:267406.
13. Lamb H (1882) On the vibrations of an elastic sphere. *Proc London Math Soc* 13: 189–212.
14. Visscher WM, Migliori A, Bell TM, Reinert RA (1991) On the normal modes of free vibration of inhomogeneous and anisotropic elastic objects. *J Acoust Am Soc* 90:2154–2162.
15. Murray DB, Laarakker AS, Saviot L (2006) High precision numerical estimates of acoustic phonon frequencies of nonspherical nanoparticles. *Phys Stat Sol (c)* 3: 3935–3938.
16. Hearmon RFS (1984) in *The Elastic Constants of Crystals and Other Anisotropic Materials*, eds Hellwege KH, Hellwege AM (Springer, Berlin), no III/18 in Landolt-Börnstein Tables, pp 1–154.
17. Stephanidis B, et al. (2007) Vibrations of nanoparticles: From nanospheres to fcc cuboctahedra. *Phys Rev B* 76:121404.
18. Ino S, Ogawa S (1967) Multiply twinned particles at earlier stages of gold film formation on alkali halide crystals. *J Phys Soc Jpn* 22:1365–1374.
19. Brust M, Walker M, Bethell D, Schiffrin DJ, Whyman R (1994) Synthesis of thiol-derivatised gold nanoparticles in a two-phase liquid-liquid system. *J Chem Soc Chem Commun* 1994:801–802.
20. Lindsay SM, Anderson MW, Sandercock JR (1981) Construction and alignment of a high performance multipass vernier tandem Fabry–Perot interferometer. *Rev Sci Instrum* 52:1478–1486.